

Self-Calibration for a 3D Laser

Mark Sheehan, Alastair Harrison, Paul Newman

Oxford University Mobile Robotics Research Group. {mcs, arh, pnewman}@robots.ox.ac.uk

Abstract—This paper describes a method for the automatic self-calibration of a 3D Laser sensor. We wish to acquire crisp point clouds and so we adopt a measure of crispness to capture point cloud quality. We then pose the calibration problem as the task of maximising point cloud quality. Concretely, we use Rényi Quadratic Entropy to measure the degree of organisation of a point cloud. By expressing this quantity as a function of key unknown system parameters, we are able to deduce a full calibration of the sensor via an online optimisation. Beyond details on the sensor design itself, we fully describe the end-to-end intrinsic parameter calibration process and the estimation of the clock skews between the constituent microprocessors. We analyse performance using real and simulated data and demonstrate robust performance over thirty test sites.

I. INTRODUCTION

The quality of data produced by a sensor is governed by the systematic and random errors inherent in its measurements. Random error is typically caused by hardware limitations of the sensor device combined with background noise from the environment. Systematic errors result in biased measurements, the detection and removal of which can be achieved by calibration. This yields data which is quantifiably more accurate. This paper concerns itself with the self calibration of one sensor in particular - a 3D laser scanner. The key idea lies in the exploitation of a closed form measure of calibration quality derived directly from the measurement stream. We place no constraints or assumptions on the sensor surroundings - it is entirely general.

Specifically we quantify the crispness of a point cloud using a measure of entropy known as Rényi Quadratic Entropy (RQE). This measure allows us to calibrate for both the geometric (*where*) and temporal (*when*) parameters of our system. This is achieved by formulating an optimisation problem. We adjust the geometric and temporal calibration parameters of our system to maximise the quality of the point cloud.

We evaluate performance of our algorithm using a 3D laser scanner built from off-the-shelf components. 2D laser sensors are ubiquitous in the field of robotics and by taking several of these sensors and rotating their scanning plane it is possible to create a 3D laser scanner at a significantly lower cost than the Velodyne laser scanner [1], with commensurate accuracy and importantly, a full field of view. We evaluate the self-calibration performance of this sensor while using our technique on 30 different test sites and demonstrate excellent repeatability.

To further validate our approach we use a simulation which generates laser scans with the same statistical noise properties as our physical device. By generating these laser scans from known ground truth calibration parameters we quantify and evaluate the accuracy of our approach.

The paper is structured as follows: Section II provides a background to this work and discusses related work. Section III describes the parametrisation of our system, outlining both the geometric and temporal calibration parameters. In Section IV we introduce the cost function used to express the quality of the point cloud. In Section V we form an optimisation problem over the calibration parameters of our system. In Section VI we discuss the results obtained and provide a quantifiable measure of the accuracy of our calibration method via simulation. We discuss our conclusions and future work in Section VII.

II. RELATED WORK

3D laser range finding sensors are becoming both popular and important in the field of mobile robots, on account of their ability to produce detailed maps of their environment as in [2], [3], [4], [5], to detect and classify objects in a scene [6], [7], as well as for segmenting moving objects from a scene [8]. Simultaneous Localisation and Mapping (SLAM) techniques have also benefited from the dense geometric representations offered by 3D range data [9], [10], [11], [12], [13]. This data can be used to model city environments by merging aerial and ground views [13], [14], as well as to recover the trajectory of a robot [5], [15].

There are three common genres of devices capable of producing 3D laser point clouds - push broom, nodder/rocker and rotational - each with their own advantages. The push broom laser is the simplest and cheapest method. A 2D laser scanner is rigidly attached to a vehicle and samples the environment as it is pushed through it. Push broom data can be gathered from a single sensor [16], [17] or gathered from multiple sensors simultaneously and then fused together [4], [18]. The drawback of such a configuration is that the lasers can only sample the environment already passed by the vehicle.

3D point clouds can also be obtained by attaching 2D laser sensors to a nodding mechanism [3], [5], [12], moving the scanning plane of the 2D sensor. However, the nodder/rocker mechanism also has drawbacks; the velocity profile of nodder mechanisms can cause the laser to spend a disproportionate amount of time sampling the extrema of its field of view (for example the ceiling and floor). In addition to this, nodding scanners typically have a limited field of view. Finally, clouds can also be created by continually rotating a planar laser sensor thus sampling the environment in a full 360° view around the laser scanner. Such sensors find application in surveying, for example an AESINGCH MStar 8000 is used in [2]. While it produces a high quality point cloud the scanner takes a long time to fully sample its environment, sampling at a rate of just 8000 points per second but at a high accuracy of

6mm range error on each scan point. In the robotics domain, both [15], [19] have attached a 2D laser scanner to a rotating mechanism allowing the 2D laser to sweep 3D volumes. The design of both of these laser scanners has greatly simplified the problem of geometric calibration by aligning the axis of rotation with the center of the scanning axis of the laser sensor. This geometric simplification is not so easy when more than one laser sensor has been used. A unique approach to 3D laser scanning is taken in [20]. Here 2D laser scans are extended to 3D by use of a rotating mirror, however this method reduces the field of view of the laser scanner and also introduces several extra unknown parameters to the system such as the mirror shape and geometry. The popular but expensive Velodyne HDL64-E [1] laser range finder uses 64 lasers on a continuously rotating head to provide high bandwidth data over an elevational range of 26.8°. It is easy to understand the popularity of this system - it is a high data rate system, producing dense point cloud data and is in some ways, a plug and play system. However, it is not without calibration issues and recently [21] describes a way of calibrating this sensor.

Our system also falls into the rotational category [22]. It employs three SICK LMS-151 laser scanning units, each with a nominal range of 50m, mounted on a spinning plate. Figure 1 shows the arrangement, which allows for 360° azimuthal coverage and almost full elevational coverage - the only unobservable volume being a cylinder through the vertical axis of rotation. While the measurement throughput of our system does not match that of the Velodyne, the field of view is much greater and measurement fidelity is superior.

Calibration tasks relating to range sensors can be broadly divided into two main categories: geometric and temporal calibration routines. Both forms of calibration are essential to achieve high measurement fidelity from a sensor on a mobile platform. There have been many previous approaches to temporal calibration. For example, in [23] a Sokuiki laser sensor is synchronised with a host computer using information from time stamps alone. Timing offsets are estimated by taking an average of the time stamps from the two devices. Clock skew estimation is sporadically compensated for, resulting in the timing calibration getting worse until re-estimation is performed again. A similar approach is taken in [24], where the issue of time synchronisation between different sensors on a robotic platform is investigated. Data and timestamps are gathered from a robot's odometry as well as from a Hokuyo URG laser range finder. In order to keep the timing offsets between the lasers and the logging PC to under 1ms they readjust their timing parameters approximately every 3 minutes. They remove the timing offset between odometry and laser measurements by comparing inferred motion from a single laser beam and odometry measurements while undergoing sinusoidal motion. A similarly bespoke timing calibration is performed in [5] by minimising the area enclosed by the curve (loop) formed by rendering only the range measurement from the forward facing beam of a nodding laser.

The problem of geometrically calibrating laser devices has typically been one of discovering the transformation between the odometry centre of a robot and a 2D laser sensor with

a single beam, often by supplying the evaluation space with bespoke calibration targets. For example [18] relies on the high remittance values of laser measurements taken from a pole covered in retro reflective tape, thus simplifying the segmentation of the pole from the environment. A cost function is devised which seeks to make the pole appear as compact as possible, when viewed from multiple vantage points. An optimisation step provides estimates of the offset and rotation between the laser sensor and the vehicles odometry centre. A similar technique is applied in [16], where retro-reflective markers are again attached to poles. This paper offers a computational efficiency increase by reposing the non-linear optimisation problem as a second order cone problem.

Multi-beam 3D laser scanning is a relatively recent development in the field of robotics and the problem of calibration has received relatively little attention. In [25] calibration parameters for the Velodyne HDL64-E are found by taking scans of a flat wall from multiple distances, a PCA technique is used to fit a plane to the data representing the wall, with a cost function devised to minimise the variance of the 3D data along a direction normal to the plane. This technique again relies on the use of a dedicated calibration target.

The most similar and recent work to our own is that of [21], which produces an excellent calibration for a Velodyne laser sensor. Both papers form a cost function which captures the overall quality of a point cloud. Similarly both papers minimise their respective cost functions by adjusting calibration parameters. In [21] these are the angular displacement and range offset between individual Velodyne laser beams and a 6DOF transform between the vehicle's IMU and the Velodyne. In our work these parameters are the poses of the laser units on the sensor's spinning plate and the timing offsets between the clocks of each laser and the logging PC. Whilst the underlying idea is the same (to maximise the quality of the point cloud), the formulation and calculation of the cost functions vary. The cost function of [21] is based on an ICP style point-to-plane metric, involving a closest-point correspondence step and local surface normal calculation from neighbouring points. Intuitively, they seek to maximize local planarity. Our method makes use of an entropy-based cost function with soft data association and no explicit computation of normals. Its large basin of convergence and minimal tuning parameters are key advantages.

Our previous work, [22] describes the design, build and automatic self-calibration of a 3D laser scanner, through the development of an entropy based cost function capturing the degree of organisation of a point cloud. The performance of the calibration routine was evaluated through the construction of a simulator which was used to generate laser scans with known true calibration parameters. In this work, we draw from [22] and expand on it. In particular, we provide a more comprehensive literature review, results from calibration experiments with data from 30 different locations, and extra simulation results. We also discuss an efficiency modification to the original cost function that results from partitioning the point clouds generated by the sensor.



Figure 1: External views of our 3D scanner, both with and without the casing attached. Our scanner employs three SICK LMS-151 laser sensors. These are 2D devices, with 0.5° angular resolution over a 270° sweep range, covered at a rate of 50Hz. Each unit makes 27,050 range measurements per second, so the total throughput of our system is 81,150 measurements per second. The LMS-151 units are mounted on a plate which rotates at speeds of up to 2.0Hz. A 12 line slip-ring supplies power and Ethernet to the rotating lasers, with a microprocessor taking encoder readings and acting as a motor controller for the plate.

III. SYSTEM PARAMETERS

While our approach is not limited to a specific design of sensor, in this paper we have applied it to the calibration of the sensor shown in Figure 1. What follows in later sections will be clearer if we use this sensor as a working example throughout the paper. In this section we shall describe a kinematic chain which, with knowledge of plate position, can be used to transform raw laser scans into a global reference frame. We also outline the methods we have used to ensure that all clocks in the system run at the same rate. This reduces the temporal calibration problem to that of discovering the timing offset between each constituent clock in the system.

A. Kinematic Chain

With reference to Figure 2, consider a laser L_i that takes measurements $\mathbf{Z}_i = \{\mathbf{z}_1 \dots \mathbf{z}_m\}$ of a set of locations, $\mathbf{X}_i = \{\mathbf{x}_1 \dots \mathbf{x}_m\}$ as it is swept around by the plate. A measurement $\mathbf{z}_j = [r_j, \theta_j, \phi_j]^T$ consists of the range r_j , the laser's mirror angle θ_j and the plate position ϕ_j . Our sensor model h_i is $\mathbf{z}_j = h_i(\mathbf{x}_j; \Theta_i)$, where $\Theta_i = [\lambda_i, \tau_i, \alpha_i]^T$ is the set of extrinsic calibration parameters for laser L_i , as shown in Figure 2. To estimate the position of the measured points given the measurements, we apply the inverse sensor model, resulting in a kinematic chain:

$$\hat{\mathbf{x}}_j = h_i^{-1}(\mathbf{z}_j; \Theta_i) \quad (1)$$

$$= \mathbf{R}_{\mathbf{z}}(\phi_j + \lambda_i) \mathbf{T}_{\mathbf{x}}(\tau_i) \mathbf{R}_{\mathbf{z}}(\alpha_i) \mathbf{R}_{\mathbf{y}}\left(\frac{\pi}{2}\right) \begin{bmatrix} r_j \cos(\theta_j) \\ r_j \sin(\theta_j) \\ 0 \end{bmatrix} \quad (2)$$

Here $\mathbf{R}_{\{\mathbf{x}, \mathbf{y}, \mathbf{z}\}}$ and $\mathbf{T}_{\{\mathbf{x}, \mathbf{y}, \mathbf{z}\}}$ are respectively, rotations about and translations along a given axis. By amalgamating a series of measurements over a period of time we are able to produce

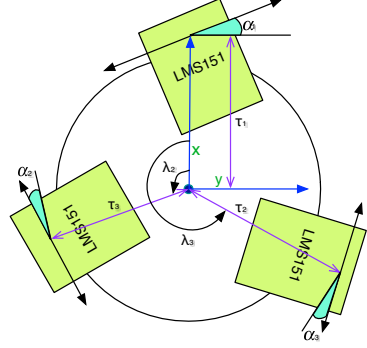


Figure 2: The location of laser L_i on the plate is defined by three parameters: τ_i is the distance of the beam origin from the centre of the plate, α_i is the angle between the laser's scanning plane and the tangent vector to the plate and λ_i is the angle subtended between beam origins as shown in the Figure. For convenience we always set $\lambda_1 = 0$. These extrinsic parameters are automatically recovered using an optimisation procedure based on maximising point cloud quality.

a 3D point cloud, $\hat{\mathbf{X}}_i = \{\hat{\mathbf{x}}_1 \dots \hat{\mathbf{x}}_m\}$ for laser L_i . Pooling measurements $\mathbf{Z} = \{\mathbf{Z}_1, \mathbf{Z}_2, \mathbf{Z}_3\}$ from all three lasers produces our final point cloud, $\hat{\mathbf{X}} = \{\hat{\mathbf{X}}_1, \hat{\mathbf{X}}_2, \hat{\mathbf{X}}_3\}$.

B. Learning the mapping between clocks

For clarity, we introduce some timing terminology. Clock offset is the difference in reported time between two clocks. The offset of clock a relative to clock b at time t is defined as $C_a(t) - C_b(t)$. Clock frequency is the rate, $C'(t)$ at which a clock runs. It will always be a positive quantity (enforcing that time does not run backwards). Skew is the difference in

frequency between two clocks. The skew of clock a relative to clock b at time t is $C'_a(t) - C'_b(t)$.

The fidelity of the measured point cloud $\hat{\mathbf{X}}$ is highly dependent on the quality of the extrinsic calibration parameters and the accuracy of the plate rotation measurements. The latter being a function of the accuracy of the time stamps on both the plate encoder measurements and the individual laser measurements. Ideally we would have some function mapping laser measurement time stamps t_j , to plate position measurements, so that $\phi_j := \phi(t_j)$, but this would unrealistically require all devices to agree on the time. In fact each LMS-151 time stamps its data using an internal clock; similarly, a microprocessor time stamps its readings of the plate encoder with its own internal clock. The situation is illustrated by Figure 3.

The clocks in consumer grade equipment are notoriously temperature sensitive and there are no guarantees of accuracy. We performed an experiment where an LMS-151 was run continuously for 5 days and its time stamps recorded. At the end of the experiment, the clock had lost over 90 seconds compared to an accurate clock measuring UTC time. This is wholly inadequate for our needs.

We could transfer all of the data to a central Hub PC and apply common time stamps upon receipt. For our application this would impose unacceptable noise, due to variable transport and buffering delays. Instead we choose to learn the mapping between the clocks on the different devices. We apply the algorithm of Moon et al. [26] to determine the relative frequency of each of the clocks relative to the clock of the Hub PC. Our implementation uses the efficient convex hull algorithm outlined in [27], which allows rapid online estimation of relative clock parameters. It operates by performing a linear programming optimisation on one-way offset measurements gathered from two clocks, which are separated by a variable delay data network. The algorithm can also recover the offset between the clocks, up to but not including the minimum transport delay, which is unobservable from one-way timing data alone.

After mapping device time stamps into Hub PC time stamps, we treat the unknown minimum transport delays as calibration parameters. η_i represents the offset between laser time stamps and plate position time stamps for the i th laser. Thus if we can determine the offsets, we can obtain the correct plate position readings for every laser measurement from a laser L_i , via the function:

$$\phi_j := \phi(t_j + \eta_i) \quad (3)$$

Sections V and VI show how the unknown offsets can be determined by considering their effect on measured point cloud quality.

IV. A MEASURE OF POINT CLOUD QUALITY

We now seek to define a measure of point cloud crispness, that will allow us to estimate the optimal calibration parameters for the system, resulting in a point cloud of high quality. Intuitively, we seek to find the calibration parameters which maximise the crispness of the point cloud.

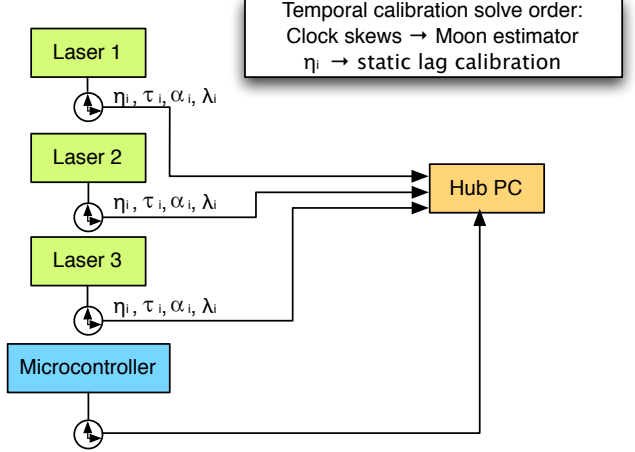


Figure 3: A laser L_i emits a stream of range and beam angle measurements time stamped according to a clock within the laser. Each laser clock is characterised by a skew relative to the clock on the hub PC and an offset η_i relative to the clock of the micro-controller. The extrinsic calibration parameters τ_i and α_i , are backed out from an analysis of plate orientation data, in conjunction with the laser range data. The solve order is as follows: The clock skews are found via the algorithm of Moon et al. [26], η_i from our static lag calibration (using nominal values of τ_i and α_i). Finally η_i is used to produce a refined estimate of τ_i and α_i for each laser. These values are then used to evaluate λ_i .

We assume that our point cloud measurements $\hat{\mathbf{X}} = \{\hat{\mathbf{x}}_1 \dots \hat{\mathbf{x}}_N\}$ are drawn from an underlying distribution, $p(\mathbf{x})$ representing the probability of drawing a measurement from a given location, \mathbf{x} . To obtain an approximation of $p(\mathbf{x})$ we apply the Parzen Window [28] density estimation method. Using a Gaussian kernel centred on each data point, we are able to represent $p(\mathbf{x})$ as a Gaussian Mixture Model (GMM),

$$p(\mathbf{x}) = \frac{1}{N} \sum_{i=1}^N G(\mathbf{x} - \hat{\mathbf{x}}_i, \sigma^2 \mathbf{I}) \quad (4)$$

where $G(\mu, \Sigma)$ is a Gaussian with mean μ and covariance Σ . An isotropic kernel is used, where $\Sigma = \sigma^2 \mathbf{I}$, with σ being our system's only tuning parameter.

The ‘crispness’ of the point cloud can now be linked to the entropy of $p(\mathbf{x})$. The more crisp the point cloud, the more ‘peaky’ the distribution $p(\mathbf{x})$ will be. An entropy measure proposed by Rényi [29] turns out to offer an efficient way to quantify the compactness of a GMM distribution [30] (as well as being a useful tool in the field of point cloud registration [31]). The Rényi entropy H_R of a stochastic variable X with pdf $p(x)$ is defined as:

$$H_R[X] = \frac{1}{1-\alpha} \log \int p(x)^\alpha dx \quad \alpha > 0, \alpha \neq 1 \quad (5)$$

The parameter α determines how event probabilities are weighted: high values of α approaching infinity consider only the highest probability events, whereas lower values of α

weight high and low probability events more equally. For the case where $\alpha \rightarrow 1$, Equation 5 becomes the familiar Shannon Entropy measure [32]. For $\alpha = 2$ we obtain:

$$H_{RQE}[X] = -\log \int p(x)^2 dx, \quad (6)$$

which is known as the Rényi Quadratic Entropy (RQE).

Substituting the Gaussian Mixture Model of Equation 4 into Equation 6 gives:

$$\begin{aligned} H_{RQE}[\hat{\mathbf{X}}] &= -\log \int \left(\frac{1}{N} \sum_{i=1}^N G(\mathbf{x} - \hat{\mathbf{x}}_i, \sigma^2 \mathbf{I}) \right)^2 d\mathbf{x} \\ &= -\log \left(\frac{1}{N^2} \sum_{i=1}^N \sum_{j=1}^N \int G(\mathbf{x} - \hat{\mathbf{x}}_i, \sigma^2 \mathbf{I}) G(\mathbf{x} - \hat{\mathbf{x}}_j, \sigma^2 \mathbf{I}) \right) d\mathbf{x}. \end{aligned} \quad (7)$$

Noting that the convolution of two Gaussians can be simplified to,

$$\int G(x - x_i, \Sigma_1) G(x - x_j, \Sigma_2) dx = G(x_i - x_j, \Sigma_1 + \Sigma_2), \quad (8)$$

we obtain a closed-form expression for the Rényi Quadratic Entropy of the GMM,

$$H_{RQE}[\hat{\mathbf{X}}] = -\log \left(\frac{1}{N^2} \sum_{i=1}^N \sum_{j=1}^N G(\hat{\mathbf{x}}_i - \hat{\mathbf{x}}_j, 2\sigma^2 \mathbf{I}) \right). \quad (9)$$

Equation 9 can be thought of as a measure of the compactness of the points in \mathbf{X} with an information-theoretic provenance, for which the only free parameter is σ . For the purposes of optimisation it is noted that the logarithm is a monotonic operator and the scale factor is unnecessary, so those terms are dropped to produce our cost function,

$$E(\hat{\mathbf{X}}) = -\sum_{i=1}^N \sum_{j=1}^N G(\hat{\mathbf{x}}_i - \hat{\mathbf{x}}_j, 2\sigma^2 \mathbf{I}), \quad (10)$$

which depends only on pairwise distances between measured points in $\hat{\mathbf{X}}$.

V. SYSTEM IDENTIFICATION

A. Formulating the optimisation problem

Substituting the inverse sensor model of Equation 1 into Equation 10, while compensating for the time lag offset corrections of Equation 3 allows the cost function to be written in terms of the extrinsic calibration parameters, $\Theta = [\Theta_1^T, \Theta_2^T, \Theta_3^T]^T$ and time stamp offset parameters $\mathbf{H} = [\eta_1, \eta_2, \eta_3]^T$, giving the cost function that we seek to optimise:

$$E(\Theta, \mathbf{H} | \mathbf{Z}) = \sum_{i=1}^N \sum_{j=1}^N G(h^{-1}(\mathbf{z}_i; \Theta, \mathbf{H}) - h^{-1}(\mathbf{z}_j; \Theta, \mathbf{H}), 2\sigma^2 \mathbf{I}). \quad (11)$$

Firstly we obtain the timing offsets \mathbf{H} . The errors caused by incorrect offset values are proportional to the angular velocity

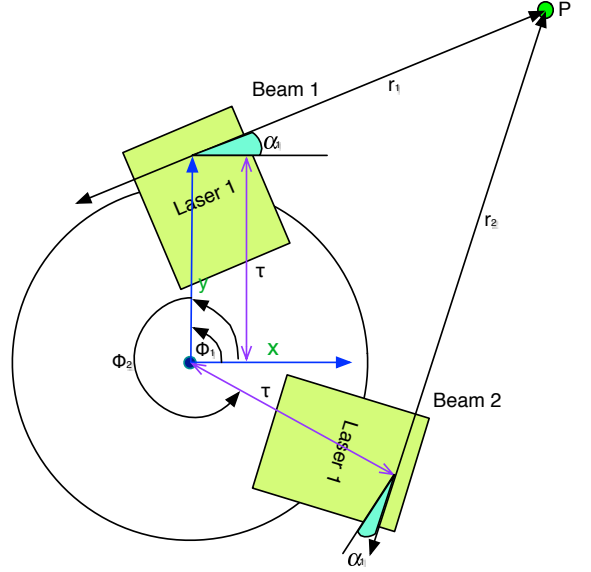


Figure 4: The geometry of a single laser scanning the same object from two different beam angles.

of the plate. In the particular case of our sensor, it is sufficient (but not necessary) to use measurements from a single beam angle in the plane of the rotating plate. Fixing τ_i and α_i to nominal values, we use a quasi-Newton method to optimise over the cost function of Equation 11,

$$\hat{\mathbf{H}} = \arg \min_{\mathbf{H}} E(\Theta, \mathbf{H} | \mathbf{Z}). \quad (12)$$

The optimisation of Equation 12 must be performed with data collected at different plate speeds. This is because at a constant speed a time lag manifests itself as a rotation in the point cloud with no distortion. However, if the plate accelerates, the point cloud twists, thereby affecting E . The larger the variation in the plate speeds, the better conditioned the calibration problem becomes.

Now that the lasers are temporally calibrated we use our values of $\hat{\mathbf{H}}$ to find $\hat{\tau}_i$ and $\hat{\alpha}_i$. At this point we require that a general point in space can be observed from two distinct sensor configurations. In our case we can see that this constraint is met by considering Figure 4 - a given point in space can be observed from both sides of the plate. Ideally, the two laser beams will sample precisely the same 3D point, though in reality this is a soft constraint – there simply needs to be some overlap between the Gaussian kernels centered on each point at the density estimation stage. The more general case (for example with a Velodyne) requires that $\hat{\mathbf{X}}$ be formed from observations from at least two known locations.

We optimise to obtain estimates of extrinsic parameters τ and α , where $\tau = [\tau_1, \tau_2, \tau_3]^T$ and $\alpha = [\alpha_1, \alpha_2, \alpha_3]^T$,

$$\hat{\tau}, \hat{\alpha} = \arg \min_{\tau, \alpha} E(\Theta, \hat{\mathbf{H}} | \mathbf{Z}) \quad (13)$$

Next we seek the relative alignment λ where $\lambda =$

$[\lambda_1, \lambda_2, \lambda_3]^T$ between the beam origins of each of the lasers. Again we use our optimised values $\hat{\boldsymbol{\tau}}, \hat{\boldsymbol{\alpha}}, \hat{\mathbf{H}}$,

$$\hat{\boldsymbol{\lambda}} = \arg \min_{\boldsymbol{\lambda}} E(\boldsymbol{\Theta}, \mathbf{H} | \mathbf{Z}) \quad (14)$$

A final optimisation over all free geometric parameters is performed to refine the crispness of the point cloud. Using previously obtained values of $\boldsymbol{\Theta}, \mathbf{H}$ to seed the optimisation,

$$\hat{\boldsymbol{\Theta}} = \arg \min_{\boldsymbol{\Theta}} E(\boldsymbol{\Theta}, \mathbf{H} | \mathbf{Z}) \quad (15)$$

Note that a system with n lasers will have $3n - 1$ geometric parameters to optimise over.

B. An Efficiency

Consider now the point clouds generated by the horizontal beams emanating from each laser. In our case we have three lasers, so six such point clouds can be built. We denote this partitioning as $\mathbf{X}^P = \{X_0^1, X_\pi^1, X_0^2, X_\pi^2, X_0^3, X_\pi^3\}$, where the superscript indicates the source laser and the subscript indicates which of the two horizontal beams are being used. Note that intuitively, it is the relationship *between* these point clouds which is important - they should completely overlap each other. That is what matters. Furthermore, note that if we optimised the RQE using just one element in the partitioning \mathbf{X} then minimisation could be achieved by shrinking τ to zero (thus reducing the overall point cloud size and by implication the RQE). Indeed, this observation lies behind the multi-view constraint described in Section V-A. These observations lead us to consider evaluating the RQE using just the cross terms between elements of \mathbf{X}^P so that the points \hat{x}_i and \hat{x}_j in Equation 9 belong to different elements of \mathbf{X}^P . We stress that it is not incorrect to use the full RQE formulation - it will still work. The RQE cost does capture the overlap between successive passes over the scene and so long as the multi-view constraint is met, inappropriate cloud shrinkage is avoided. It is simply that one can remove from the overall cost the effects of point-to-point pairings which cannot usefully influence convergence.

We can now state a modified form of the objective function. Recall that our original analysis considered the laser measurements to be a Gaussian kernel in a Parzen approximation to an underlying p.d.f. If, as already described, we partition \mathbf{X} into subsets of point clouds (and by implication p.d.f's) we can write

$$E(\mathbf{X} | \boldsymbol{\Theta}, \mathbf{H}) = \sum_{\{P, Q\}} \sum_i \sum_j G(\mathbf{p}_i - \mathbf{q}_j, 2\sigma^2 \mathbf{I}) \quad (16)$$

where $\mathbf{P}, \mathbf{Q} \in \mathbf{X}^P, \mathbf{P} \neq \mathbf{Q}$

which is a sum over the weighted exponentiated distances between all possible points in pairings of subsets of \mathbf{X}^P .

VI. RESULTS

In this section we investigate the outcomes of our calibration process using both real and simulated data.

Variable	Mean	Standard Deviation
$\hat{\tau}_1$	0.1979 m	0.0029 m
$\hat{\tau}_2$	0.1991 m	0.0033 m
$\hat{\tau}_3$	0.2027 m	0.0019 m
$\hat{\alpha}_1$	-0.7014°	0.3081°
$\hat{\alpha}_2$	-0.1836°	0.1787°
$\hat{\alpha}_3$	0.7529°	0.1693°
$\hat{\lambda}_1$	118.1625°	0.2676°
$\hat{\lambda}_2$	239.2594°	0.3942°

Table I: Calibration statistics obtained from from real data acquired from our 3D laser scanning system from 30 different locations

A. Results from real data

To test our calibration method we have applied our calibration approach to real data collected from our 3D laser scanner, shown in Figure 1 at 30 different locations around our laboratory complex, this dataset contains office spaces, laboratories, and corridor segments. Estimates for spatial and temporal parameters were obtained from Equations 12, 13 and 14. Our aim is to show that our approach is robust to the structure of the scene in which calibration is occurring. While it is not possible to provide the mean error for these results as the ground truth calibration parameters for our laser are unknown (that after all is what motivates this work), we provide the mean and standard deviation of the estimates in Table I along with box-plots in Figure 6 to illustrate their spread.

1) *Timing Calibration*: Figure 5 shows two planar point clouds created from a single horizontal beam while the plate frequency was varied between 0 and 2Hz. One plot is generated assuming zero timing offset, $\eta_i = 0$ and the other for the deduced optimal lag value $\eta_i = \hat{\eta}_i$ obtained from the optimisation of Equation 12.

Figure 6d shows the spread of η_i for all three lasers with the mean value subtracted. The boxes span the 25th and 75th percentiles. There is no single correct value of η , as the timing offset value will be different each time the system is started, however we note that no timing offsets lie more than 2 milliseconds from the mean, indicating that both our system and our timing calibration routine perform with consistent timing offset.

2) *Geometric Calibration*: Table I shows statistics resulting from running our procedure on data from the 30 test sites. The radial terms τ show a 3mm standard deviation which is perhaps larger than one would hope for but looking at the box plots in Figure 6 we can see this is attributable in part to just a few outliers - perhaps due to environments which cause a large number of mixed measurements. The angular parameters are very consistent, which speaks for the fact that these parameters have a marked effect on the point cloud quality - in contrast changing the plate radius τ a few mm has a proportionally smaller effect on point cloud entropy.

Figure 6 shows the spread of the geometric parameters around their mean value. The boxes span the 25th and 75th percentiles.

3) *Convergence*: Figure 7 shows a contour plot of the cost surface generated in Equation 13 using real data. The cost

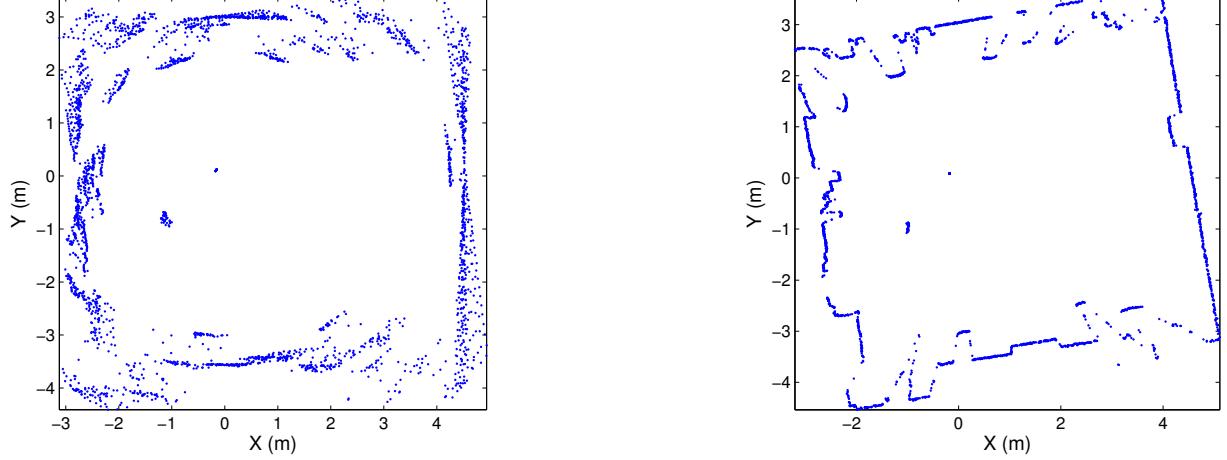


Figure 5: The effect of timing errors. Real data from a single horizontal laser beam taken with the plate running between frequencies of 0Hz and 2.0Hz. The left image shows the points with an assumed lag of $\hat{\eta} = 0\text{ms}$ and the right image with $\hat{\eta} = 38\text{ms}$.

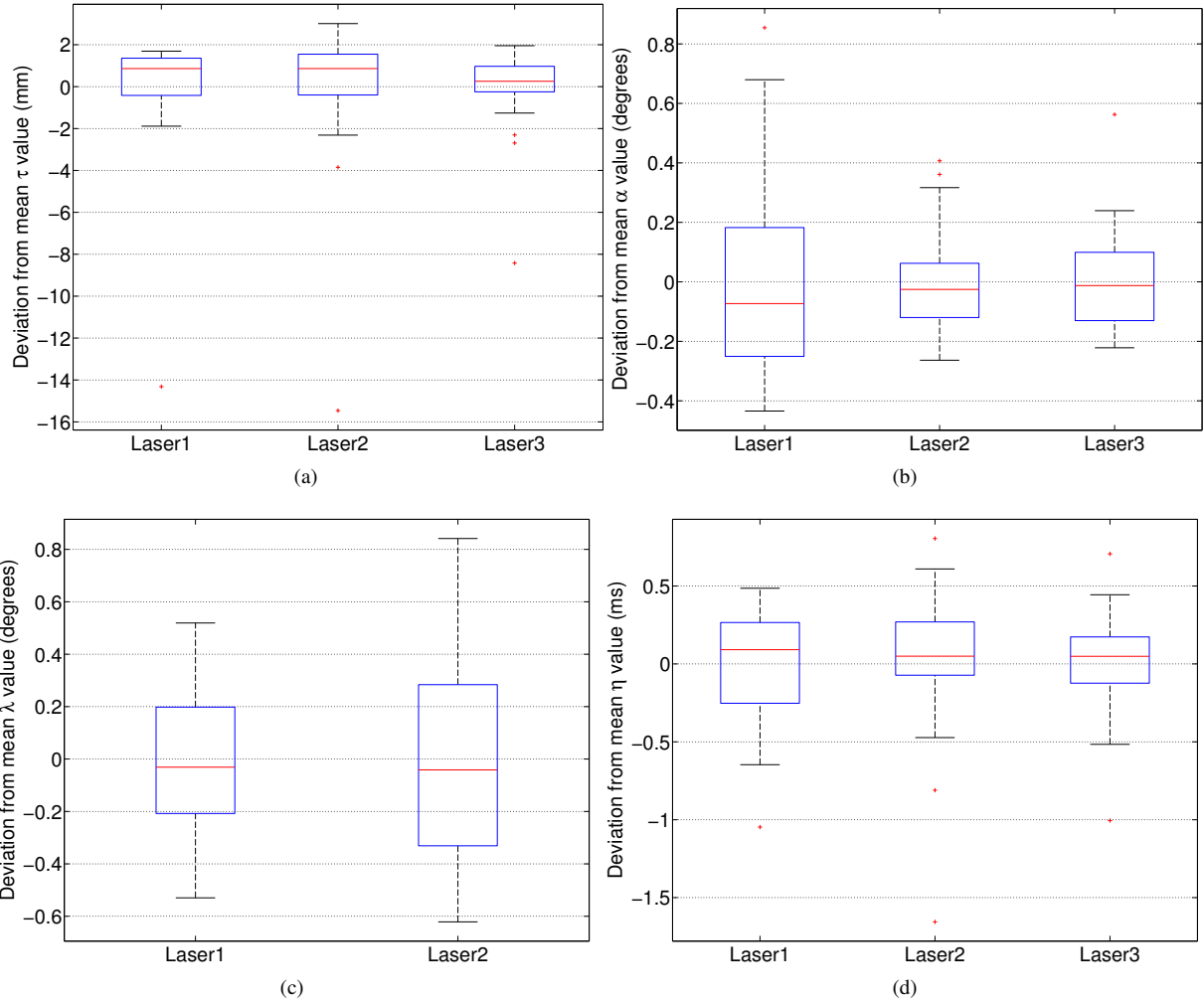


Figure 6: Deviation of our calibration results from their mean values, our data was obtained from 30 different locations around our laboratory complex. The results are depicted using box plots to highlight the spread of the data. The boxes span the 25th and 75th percentiles, with the median depicted by the central line in the box plot. The tails of the box plots represent the range.

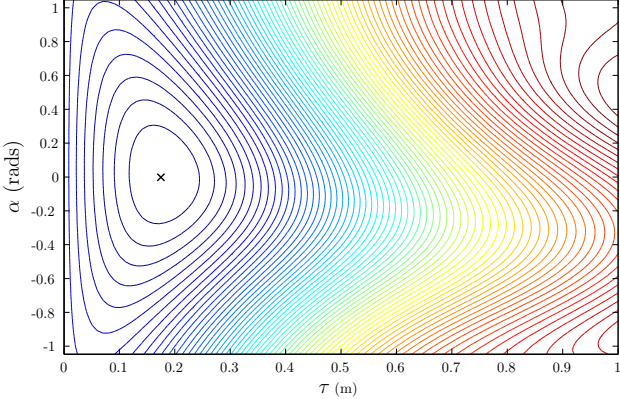


Figure 7: Contour plot of cost surface $E(\Theta, H|Z)$ generated using real laser data evaluated over a range of τ and α values. A cross is used to depict the minimum.

Variable	Mean error	Standard Deviation
τ	2.1mm	0.6mm
α	0.06°	0.12°
λ	0.0009°	0.0322°
η	441 μ s	402 μ s

Table II: Deviance of results from ground truth values.

surface can be seen to have a reasonable basin of convergence, with a single minimum even with up to a meter of error in τ and one radian of error in α .

B. Performance Verification

Given the lack of ground truth values for our calibration parameters it is hard to numerically quantify the accuracy of our results. To show that our calibration procedures estimate the true underlying parameters and to provide quantifiable accuracy, we use a series of Monte-Carlo simulations using synthetic laser data. Our simulator generates measurements z_i polluted by additive noise $N_z \sim N(0, \sigma_z^2)$ with $\sigma_z = 0.012$ m to match the statistical noise of the real laser measurements (from [33]) and with system parameters set to $\eta = 30$ ms, $\tau_{true} = 0.20$ m, $\alpha_{true} = 0^\circ$ and $\lambda_{true} = 120^\circ, 240^\circ$ respectively, 1500 simulated runs were performed. Table II shows the results of these tests. λ converged to an error range of 0.22° for all 1500 runs despite being seeded with a worst case value of $\lambda = 180^\circ$. τ had an error range of 0.004m, α had an error range of 1 degree and the temporal lag η has a mean error of just 400 μ s.

C. Selection of free parameter (σ)

We also leverage the simulation to show how variation of the free parameter σ affects our estimates of calibration parameters by varying σ between 0.1 and 2m. Figure 8 shows that estimates of τ and α become increasingly inaccurate with larger values of σ , this motivates setting σ to a small value. On the other hand consider Figure 9, which shows the behaviour of the objective function $-E$ as a function of timing lag for different values of σ . We see that as σ decreases the cost function becomes more ‘peaky’. At very

small values many local minima are introduced to the cost function making optimisation challenging. In the limit the cost function degenerates into a set of delta functions. Practically we choose an initial value of σ which is significantly larger (times 10) than the noise in the measurements, providing a cost function with a large basin of convergence, which can be optimised to give an initial calibration estimate. This estimate can then be used to seed a subsequent optimisation with a value of σ close to the measurement noise of the system. It is not a requirement to use different values of σ . But if the true calibration value is truly unknown the calibration procedure can be run once with a large convergence basin (large value of σ) to obtain a good estimate of the parameter(s) and then ran again with a smaller value of σ to obtain a more accurate result. A typical calibration process consists of two optimisations, each with a different values of sigma.

D. Computational Performance and run times

Interpreting Equation 16 literally, gives our cost function a computational complexity of $O(N^2)$, where N is the number of points in the point cloud. As Geometric calibration only needs to be performed when the sensor is reconfigured, only the temporal calibration routine needs to be run on powering up the sensor. On a single core of a 2.66Ghz Core2Duo processor, our implementation in Matlab typically takes around 2 seconds of computation per laser. We find that 15 seconds of gathered data is generally sufficient, with the optimisation taking around 5 iterations to converge.

We have shown that it is perfectly feasible to compute the entropy using the full $O(N^2)$ cost function and therefore calibrate the system on-line. If required, the cost could be substantially reduced by using an efficient search structure such as a kd-tree [34]. This exploits the property that our cost function is inherently sparse; distant point pairs have negligible impact on the overall entropy. Using such a scheme, the computational complexity can be reduced to $O(kN \log N)$, where k is the local neighbourhood size.

E. Discussion

Having calibrated our system, we provide examples of generated point clouds. Figure 10 shows data taken from an indoor office environment while rotating at 1Hz and Figure 11 shows a typical outdoor scene. Qualitatively the images appear crisp, as the RQE measure has been optimised over all extrinsic calibration parameters for each point cloud. We stress that the point of this paper is not subjectively fine images but objectively crisp point clouds as demonstrated from the previous figures and tables.

Our algorithm performs excellently in regions containing planar or non-planar surfaces, requiring only that the environment is well represented by the samples. Due to the diameter of the laser spots in our particular sensor, areas of foliage are not well represented and tend to generate many spurious measurements.

We have found that the accuracy of the geometric calibration parameters is sensitive to even a small error (>1ms) in the temporal calibration values. This is because of the pronounced

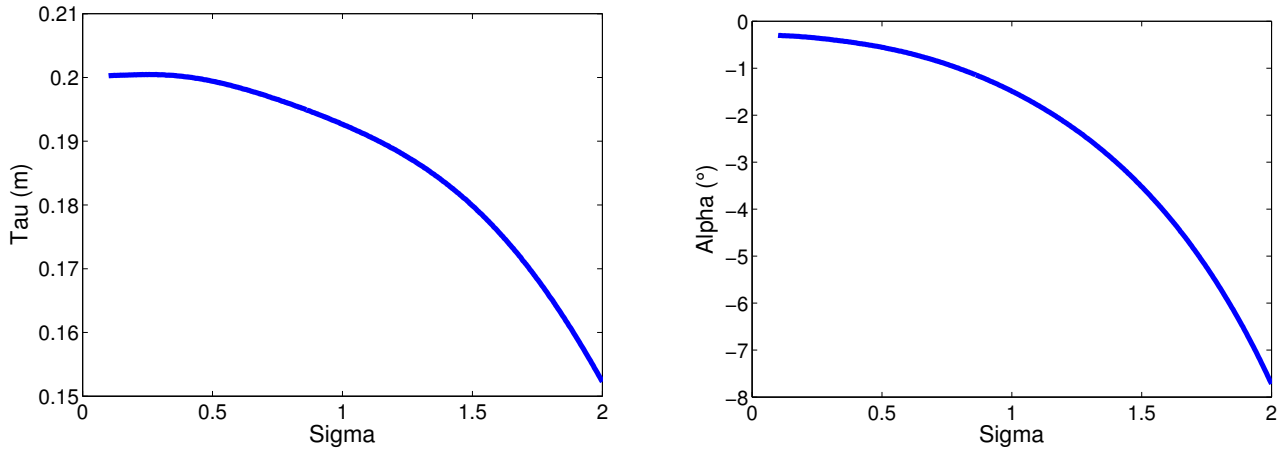


Figure 8: Variation of calibration parameters α and τ with free parameter σ where $\tau_{true} = 0.2\text{m}$ and $\alpha_{true} = 0^\circ$

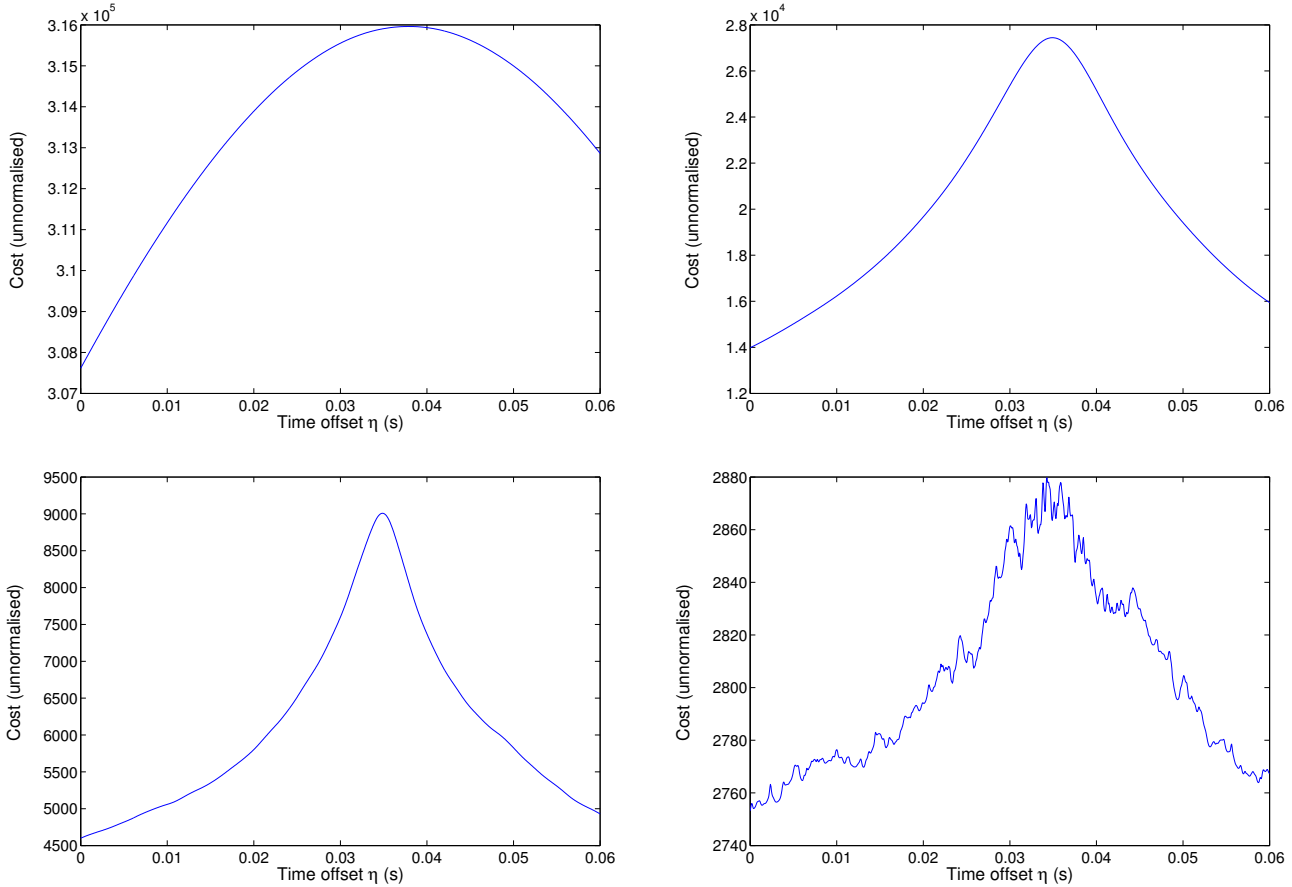


Figure 9: The variation of the cost function of Equation 12 with free parameter σ for real laser data. Using σ values of: top left 0.5m , top right 0.04m , bottom left 0.012m , bottom right 0.001m . Clearly a value of 0.001m is too low for successful optimisation, since the basin of convergence is too small - close neighbouring points have insufficient influence on the cost function.



Figure 10: A crisp point cloud of our lab generated using optimised values $\hat{\Theta}$ and \hat{H} . Point colouring is based on laser reflectance values. This point cloud was achieved at a plate speed of 1Hz.

smearing effect that incorrect lag values have on the point cloud (Figure 5). This highlights the importance of good temporal calibration.

The standard deviation of our calibration results from simulated data is slightly lower than that of our results from real data. There are a few reasons why this could be: firstly the quality of the simulated data is better than that of the data from the laser scanner. In addition, laser scanners can suffer from a phenomenon known as mixed measurements [35], where spurious range measurements are produced by the reflection of a laser beam from two different surfaces. This effect was not simulated and although we have filtered our data for these measurements some still remain and detract from the overall quality of the point cloud.

Nevertheless, the calibration process produces good results, with a low spread in calibration parameter values across all test sites.

VII. CONCLUSIONS

In this paper we have described our new 3D laser scanner, which has a full field of view. We have formed a cost function

which describes the quality of a point cloud from first principles. This is achieved by treating the point cloud measurements as samples drawn from a pdf covering the true underlying environment. By forming a Gaussian Mixture Model over these samples we obtain a probabilistic interpretation of the underlying structure of the environment. By evaluating and minimising the Rényi Quadratic Entropy of this distribution we obtain optimal calibration parameters. We have shown that our formulation provides consistent calibration values across scenes with a low variance. Through the use of a Monte-Carlo simulator we have quantified its accuracy.

A. Future Work

In Section VI-C we outlined how the convexity of the cost function varies with free calibration parameter σ . We have used a single value of σ throughout the paper. Although this is the only parameter to our system we believe that by intelligently varying the value of σ across the point cloud - for example, by increasing it in regions where the points are more sparse we can obtain a better estimation of the underlying probability distribution. We have also evaluated our



Figure 11: A point cloud generated of a typical outdoor environment. Visualised a few meters from the laser scanner. Plate speed 1Hz

Gaussians with a fixed spherical shape of $\sigma^2\mathbf{I}$. We are currently investigating how this spherical model could be replaced with an alternative which captures indications of the local surface properties. These are implicit from the local shape of the point cloud. Given that we already know σ can have a substantial effect on performance. Our sense is that modulating σ appropriately will produce a further improvement in precision. This is ongoing work.

Acknowledgements

This work has been sponsored by Guidance Ltd and by the European Commission under grant agreement number FP7-231888-EUROPA. Thanks to Navtech Radar Ltd for supplying the plate hardware.

REFERENCES

- [1] V. Acoustics, *Velodyne's HDL-64E: A High Definition Lidar Sensor for 3-D Applications*, 2007.
- [2] S. Hu and A. Zhang, "3D laser omnimap for 3D reconstruction of large-scale scenes," in *Urban Remote Sensing Event, 2009 Joint*, pp. 1–5, May 2009.
- [3] Z. Keqiang, Z. Yan, and W. Wei, "Automated 3D scenes reconstruction for mobile robots using laser scanning," in *Control and Decision Conference, 2009. CCDC'09. Chinese*, pp. 3007–3012, IEEE, 2009.
- [4] J. Levinson, M. Montemerlo, and S. Thrun, "Map-based precision vehicle localization in urban environments," in *Proceedings of Robotics: Science and Systems*, (Atlanta, GA, USA), June 2007.
- [5] A. Harrison and P. Newman, "High quality 3D laser ranging under general vehicle motion," in *Robotics and Automation, 2008. ICRA 2008. IEEE International Conference on*, pp. 7–12, IEEE, 2008.
- [6] F. Endres, C. Plagemann, C. Stachniss, and W. Burgard, "Unsupervised Discovery of Object Classes from Range Data using Latent Dirichlet Allocation," in *Proceedings of RSS 2009, Seattle, WA, USA*, pp. 113–120, Citeseer, 2009.
- [7] K. Lai and D. Fox, "3D laser scan classification using web data and domain adaptation," in *Proc. of Robotics: Science and Systems (RSS)*, Citeseer, 2009.
- [8] D. Steinhauser, O. Ruepp, and D. Burschka, "Motion segmentation and scene classification from 3D LIDAR data," in *Intelligent Vehicles Symposium, 2008 IEEE*, pp. 398–403, IEEE, 2008.
- [9] D. Cole, A. Harrison, and P. Newman, "Using naturally salient regions for SLAM with 3D laser data," in *International Conference on Robotics and Automation, SLAM Workshop*, Citeseer, 2005.
- [10] N. Fairfield, *Localization, mapping, and planning in 3D environments*. PhD thesis, PhD thesis, Carnegie Mellon University, Pittsburgh, PA, USA, 2009, Jan 2009.
- [11] A. Nuchter, K. Lingemann, J. Hertzberg, and H. Surmann, "6D

Symbol	Meaning
L_i	The i th laser
r_j	The j th range measurement from a laser
θ_j	The j th angle measurement from a laser
ϕ_j	The j th orientation measurement from the encoder
τ_i	The distance from the rotational axis of the disc to the beam origin of the i th laser
α_i	The angle between the scanning plane of the i th laser and the tangent to the plate
λ_i	The angle between the i th beam origin and the first beam origin along plate radials
Θ_i	The geometric calibration parameters for the i th laser $\lambda_i, \tau_i, \alpha_i$
η_i	The timing offset between the i th laser and the encoder measurements
H_{RQE}	The Rényi Quadratic Entropy
$E(\hat{\mathbf{X}})$	Our cost function based on Rényi Quadratic Entropy
σ	Free parameter changing the standard deviation of Gaussian kernels used in the mixture model

Table III: List of parameters provided for reference.

- SLAM with approximate data association,” in *Advanced Robotics, 2005. ICAR’05. Proceedings., 12th International Conference on*, pp. 242–249, IEEE, 2005.
- [12] R. Valencia, E. Teniente, E. Trulls, and J. Andrade-Cetto, “3D mapping for urban service robots,” in *Intelligent Robots and Systems, 2009. IROS 2009. IEEE/RSJ International Conference on*, pp. 3076 –3081, 2009.
- [13] R. Kümmerle, B. Steder, C. Dornhege, A. Kleiner, G. Grisetti, and W. Burgard, “Large scale graph-based slam using aerial images as prior information,” *Autonomous Robots*, vol. 30, pp. 25–39, 2011.
- [14] C. Früh and A. Zakhor, “Constructing 3D city models by merging aerial and ground views,” *Computer Graphics and Applications, IEEE*, vol. 23, no. 6, pp. 52 – 61, 2003.
- [15] M. Bosse and R. Zlot, “Continuous 3D scan-matching with a spinning 2D laser,” in *ICRA’09. IEEE International Conference on Robotics and Automation*, pp. 4312–4319, IEEE, 2009.
- [16] C. Gao and J. Spletzer, “On-line calibration of multiple LIDARs on a mobile vehicle platform,” in *Robotics and Automation (ICRA), 2010 IEEE International Conference on*, pp. 279–284, IEEE, 2010.
- [17] R. Kaushik, J. Xiao, W. Morris, and Z. Zhu, “3D laser scan registration of dual-robot system using vision,” in *Intelligent Robots and Systems, 2009. IROS 2009. IEEE/RSJ International Conference on*, pp. 4148 – 4153, 2009.
- [18] J. Underwood, A. Hill, T. Peynot, and S. Scheding, “Error modeling and calibration of exteroceptive sensors for accurate mapping applications,” *Journal of Field Robotics*, vol. 27, no. 1, pp. 2–20, 2010.
- [19] T. Ueda, H. Kawata, T. Tomizawa, A. Ohya, and S. Yuta, “Mobile SOKUIKI Sensor System: Accurate Range Data Mapping System with Sensor Motion,” in *International Conference on Autonomous Robots and Agents*, 2006.
- [20] J. Ryde and H. Hu, “3D laser range scanner with hemispherical field of view for robot navigation,” in *Advanced Intelligent Mechatronics, 2008. AIM 2008. IEEE/ASME International Conference on*, pp. 891–896, IEEE, 2008.
- [21] J. Levinson and S. Thrun, “Unsupervised calibration for multi-beam lasers,” in *In Proceedings of the International Symposium on Experimental Robotics (ISER)*, 2010.
- [22] M. Sheehan, A. Harrison, and P. Newman, “Automatic self-calibration of a full field-of-view 3D n-laser scanner,” in *In Proceedings of the International Symposium on Experimental Robotics (ISER2010)*, (New Delhi and Agra, India), December 2010.
- [23] A. Carballo, Y. Hara, H. Kawata, T. Yoshida, A. Ohya, and S. Yuta, “Time synchronization between SOKUIKI sensor and host computer using timestamps,” in *Multisensor Fusion and Integration for Intelligent Systems, 2008. MFI 2008. IEEE International Conference on*, pp. 261–266, IEEE, 2007.
- [24] F. Tungadi and L. Kleeman, “Time Synchronisation and Calibration of Odometry and Range Sensors for High-Speed Mobile Robot Mapping,” in *Proc. Australasian Conf. Robotics and Automation (ACRA’08)*, J. Kim and R. Mahony, Eds., Canberra, Australia, 2008.
- [25] N. Muhammad and S. Lacroix, “Calibration of a rotating multi-beam lidar,” in *Intelligent Robots and Systems (IROS), 2010 IEEE/RSJ International Conference on*, pp. 5648–5653, IEEE, 2010.
- [26] S. Moon, P. Skelly, and D. Towsley, “Estimation and removal of clock skew from network delay measurements,” *INFOCOM ’99. Eighteenth Annual Joint Conference of the IEEE Computer and Communications Societies. Proceedings. IEEE*, vol. 1, pp. 227–234 vol.1, 1999.
- [27] L. Zhang, Z. Liu, and C. H. Xia, “Clock synchronization algorithms for network measurements,” *INFOCOM 2002. Twenty-First Annual Joint Conference of the IEEE Computer and Communications Societies. Proceedings. IEEE*, vol. 1, pp. 160–169 vol.1, 2002.
- [28] E. Parzen, “On estimation of a probability density function and mode,” *The annals of mathematical statistics*, vol. 33, pp. 1065–1076, Jan 1962.
- [29] A. Rényi, “On measures of entropy and information,” in *Fourth Berkeley Symposium on Mathematical Statistics and Probability*, pp. 547–561, 1961.
- [30] J. Principe and D. Xu, “Learning from examples with renyi’s information criterion,” in *Signals, Systems, and Computers, 1999. Conference Record of the Thirty-Third Asilomar Conference on*, vol. 2, pp. 966 –970 vol.2, 1999.
- [31] Y. Tsai and T. Kanade, “A correlation-based approach to robust point set registration,” in *Computer Vision-ECCV 2004*, pp. 558–569, Springer, 2004.
- [32] C. Shannon, “A Mathematical Theory of Communication,” *Bell System Technical Journal*, vol. 27, pp. 379–423, July/October 1948.
- [33] *Operating instructions - LMS100/111/120/151 Laser Measurement Systems*.
- [34] J. Friedman, J. Bentley, and R. Finkel, “An algorithm for finding best matches in logarithmic expected time,” *ACM Transactions on Mathematical Software (TOMS)*, vol. 3, no. 3, pp. 209–226, 1977.
- [35] P. Skrzypczynski, “How to recognize and remove qualitative errors in time-of-flight laser range measurements,” in *Intelligent Robots and Systems, 2008. IROS 2008. IEEE/RSJ International Conference on*, pp. 2958–2963, IEEE, 2008.